A benthic δ^{13}C-based proxy for atmospheric pCO_2 over the last 1.5 Myr

Auxiliary material

Lorraine E. Lisiecki

Department of Earth Science, University of California, Santa Barbara

1 δ^{13}C stacks and gradients

The δ^{13}C records used in this study are collected from previous studies and primarily measured from the epibenthic taxon Cibicidoides wuellerstorfi. All records are placed on a common age model by aligning their benthic δ^{18}O records to the LR04 benthic δ^{18}O stack [Lisiecki and Raymo, 2005]. After alignment, benthic δ^{13}C records are interpolated at even 2-kyr time steps and averaged together to produce regional stacks [Lisiecki, 2010]. Auxiliary Table S1 lists the cores used for each stack. All North Atlantic and Pacific records span the entire interval from 0-1.5 Ma except for ODP 552 which spans 0-1.3 Ma and ODP 806B which spans 0-750 ka. Constant values of 0.06‰ and 0.02‰ are added to the North Atlantic and Pacific stacks, respectively, after these cores end to correct for the small differences between the mean δ^{13}C value of these cores and the others in the stack. Before calculating δ^{13}C gradients, the North Atlantic stack is smoothed with a 4-kyr boxcar filter to compensate for correlation uncertainites between the Atlantic and Pacific [Lisiecki and Raymo, 2009].

There are several reasons why the Pacific δ^{13}C stack is used instead of the deep South Atlantic stack when calculating the deep-intermediate δ^{13}C gradient. First, North Atlantic Deep Water (NADW) boundary movement affects South Atlantic δ^{13}C but not deep Pacific δ^{13}C [Matsumoto et al, 2002;

Lisiecki, 2010]. Second, only one deep South Atlantic record is available beyond 850 ka whereas three Pacific δ^{13}C records are available back to 1.5 Ma, thus, improving the signal-to-noise ratio. Third, the deep Pacific has more than four times the volume of the deep South Atlantic, and thus may store more ΣCO_2 despite the fact that the amplitude of δ^{13}C change is smaller in the Pacific. Finally, $\Delta\delta^{13}C_{P-\frac{NA}{2}}$ (r=0.75) correlates better with pCO_2 than $\Delta\delta^{13}C_{SA-NA}$ (r=0.65) or $\Delta\delta^{13}C_{SA-\frac{NA}{2}}$ (r=0.70).

Glacial-interglacial changes in deep Pacific δ^{13}C appear to contain a record of changes in the vertical ΣCO_2 gradient in addition to a terrestrial biomass signal. The LGM-Holocene δ^{13}C change in the deep Pacific stack is 0.4‰ whereas mean ocean δ^{13}C change is 0.3‰ [Duplessy et al, 1988]. Deep Pacific δ^{13}C can differ significantly from mean ocean δ^{13}C because the deep Pacific ($\geq$2500 m) constitutes 23% of ocean volume whereas water shallower than 2500 m (globally) constitutes 56% of ocean volume. For the last 800 kyr, deep Pacific δ^{13}C values are consistent with a constant mixture of 60% North Atlantic δ^{13}C and 40% deep South Atlantic δ^{13}C and a constant remineralization/age offset of -0.5‰ [Lisiecki, 2010]. Subtracting the North Atlantic intermediate stack from the deep Pacific stack should emphasize the portion of the Pacific δ^{13}C signal related to ΣCO_2 vertical gradients and remove much of the mean-ocean δ^{13}C signal.

The decision to subtract half the North Atlantic stack is based on the empirical agreement between $\Delta\delta^{13}C_{P-\frac{NA}{2}}$ and pCO_2. One possible physical interpretation of $\Delta\delta^{13}C_{P-\frac{NA}{2}}$ (or equivalently $\Delta\delta^{13}C_{2P-NA}$) is that it represents the deep-intermediate $\delta^{13}C$ gradient within the Atlantic because twice the Pacific stack is a good proxy for deep South Atlantic $\delta^{13}C$. The South Atlantic $\delta^{13}C$ stack is not used directly because it is also affected by changes in %NADW [Venz and Hodell, 2002]. Alternatively, the good correlation between $\Delta\delta^{13}C_{P-\frac{NA}{2}}$ and pCO_2 might suggest that temperature and/or circulation changes in the intermediate North Atlantic amplify the mean ΣCO_2 signal of the surface/intermediate ocean.

2 Uncertainties in pCO_2 estimates

Uncertainty in the regional $\delta^{13}C$ stacks at each time step is estimated based on the standard error of the interpolated $\delta^{13}C$ values from the component cores. Then, the 1-σ uncertainty of $\Delta\delta^{13}C_{P-\frac{NA}{2}}$ is calculated from the combined contributions of the standard errors of the Pacific stack and half the Atlantic stack (Figure S1). $\Delta\delta^{13}C_{P-\frac{NA}{2}}$ has a 1-σ uncertainty of 0.11‰ from 0.8–0 Ma and 0.13‰ from 1.5–0.8 Ma (equivalent to 17.5 ppm and 19.2 ppm, respectively). The uncertainty is larger for the older interval because the ODP 806B record ends at 750 ka, and the ODP 552 record ends at 1.3

Ma.

Interestingly, the LR04 benthic δ^{18}O stack has a slightly better correlation with pCO_2 (r=-0.83) than $\Delta\delta^{13}C_{P-\frac{NA}{2}}$ does (r=0.75). However, this is likely an artifact of the higher signal-to-noise ratio of the δ^{18}O stack of 57 sites (standard error = 0.06‰).

To generate pCO_2 estimates from $\Delta\delta^{13}C_{P-\frac{NA}{2}}$, the proxy is scaled to have the same mean and standard deviation from 0.8–0 ka as ice core pCO_2, after the pCO_2 record has been smoothed with a 2-kyr boxcar filter and interpolated to the same 2-kyr resolution as $\Delta\delta^{13}C_{P-\frac{NA}{2}}$. This produces the conversion: $pCO_2 = 161.5 \frac{ppm}{‰} \times \Delta\delta^{13}C_{P-\frac{NA}{2}} + 219.5$ ppm. The root mean square error (RMSE), calculated from the residuals between $\Delta\delta^{13}C_{P-\frac{NA}{2}}$ and the smoothed ice core pCO_2 record, is 17.5 ppm (n=397). RMSE values for the boron-based estimates are calculated using residuals from smoothed, interpolated pCO_2 values. Note that all of the RMSE values include the effects of age model uncertainty. The boron-based estimates have RMSE of 18.1 ppm (n=25) [Hönisch et al., 2009] and 24.9 ppm (n=42) [Tripati et al., 2009]. (The originally published RMSE for pCO_2 estimates from Tripati et al. [2009] were in error [personal communication, A. Tripati, Sept. 2010].) Thus, the empirically derived $\Delta\delta^{13}C_{P-\frac{NA}{2}}$ proxy appears to agree with ice core pCO_2 at least as well as the physically derived boron-based proxies.

3 Calculations of lags and spectral power

For correlation, RMSE, and phase calculations, the pCO_2 record is analyzed on the EDC3_gas_a age model [Loulergue et al, 2007], smoothed with a 2-kyr boxcar filter, and interpolated to an even 2-kyr time step. Termination lags between proxies are calculated using 15–30 kyr windows centered on each termination (Tables S2 and S3), shifting one proxy by -11 to +11 kyr in increments of 0.1 kyr, and determining which shift produces the best correlation. This procedure favors the alignment of termination midpoints but is also affected to a lesser extent by suborbital-scale features of the signals. Lags are estimated for the alkenone concentration proxy using an age model based on the alignment of ODP 1090 planktonic $\delta^{18}O$ to the LR04 benthic $\delta^{18}O$ stack (see Auxiliary Section 4).

The lags between $\Delta\delta^{13}C_{P\_\frac{NA}{2}}$ and pCO_2 (Table S2) estimate the age difference between abrupt pCO_2 change in the EDC_gas_a and LR04 age models. These lags should be interpreted as differences between the independently derived age models rather than as lags between climate responses. Estimates of the amount of time between pCO_2 and ice volume change are provided by the lag between $\Delta\delta^{13}C_{P\_\frac{NA}{2}}$ and $\delta^{18}O$ (Table S3). Because $\delta^{13}C$ and $\delta^{18}O$ are both recorded in marine sediments, these phase lags do not depend on agreement between the ice core and marine sediment age

models.

$\Delta\delta^{13}C_{P-\frac{NA}{2}}$ lags benthic $\delta^{18}O$ by $\geq$3 kyr during Termination 6 and MIS 18. A lag between benthic $\delta^{13}C$ and $\delta^{18}O$ during these two time periods is also visible in each Pacific core (Figure S2). At these times the phase difference between Pacific $\delta^{13}C$ and $\Delta\delta^{13}C_{P-\frac{NA}{2}}$ is minimal (Figure 1b). Although individual records are noisier than stacked data, in all four cores Termination 6 ends and the $\delta^{18}O$ trend reverses before $\delta^{13}C$ reaches its interglacial maximum. MIS 18 is only partially recorded in ODP 806B, but in the other cores $\delta^{18}O$ reaches its warm substage plateau while $\delta^{13}C$ is still near its glacial minimum.

The responses of pCO_2, $\Delta\delta^{13}C_{P-\frac{NA}{2}}$, and $\delta^{18}O$ are also compared using wavelet power spectra and cross-wavelet analysis with MATLAB codes written by Torrence, Compo and Grinsted [Grinsted et al, 2004]. The wavelet power spectra of $\Delta\delta^{13}C_{P-\frac{NA}{2}}$ and pCO_2 are similar from 0-800 ka and coherent at the 41- and 100-kyr periods except for two intervals of relatively weak 41-kyr power at 400-500 ka and $\sim$700 ka (Figure S3). Phase estimates between the two are not reliable because the two time series are on different age models.

The phase between $\Delta\delta^{13}C_{P-\frac{NA}{2}}$ and benthic $\delta^{18}O$ can be calculated with confidence because both are measured in marine sediments. The 100-kyr

cycle of the two has a coherence of at least 0.85 since 900 ka; the 100-kyr phase lag of δ^{18}O decreases from 18 kyr before 800 ka to 5-10 kyr from 750–0 ka (Figure S4b). However, changes in the 100-kyr lag may be more representative of differences in the shape of glacial cycles (i.e., a more pronounced saw-tooth shape in benthic δ^{18}O than $\Delta\delta^{13}C_{P-\frac{NA}{2}}$) than the timing of abrupt changes. Coherence in the 41-kyr band is only greater than 0.85 during three short intervals. Since 1.1 Ma the 41-kyr response of benthic δ^{18}O has lagged $\Delta\delta^{13}C_{P-\frac{NA}{2}}$ by 0–1 kyr when coherent. Before 1.2 Ma δ^{18}O leads $\Delta\delta^{13}C_{P-\frac{NA}{2}}$ by 2–4 kyr. The two failed terminations (T6 and MIS 18) occur during an interval of particularly low 41-kyr coherence from 750–500 ka, which coincides with a minimum in the power of obliquity forcing.

4 Age model for ODP 1090

Here I compare several possible age models for the alkenone concentration proxy from ODP 1090. An age model based on alignment of ODP 1090 benthic δ^{18}O to the LR04 benthic δ^{18}O stack would ordinarily be considered the most reliable age model for comparing the alkenone proxy to $\Delta\delta^{13}C_{P-\frac{NA}{2}}$. However, the lag between $\Delta\delta^{13}C_{P-\frac{NA}{2}}$ and benthic δ^{18}O during the two failed terminations suggests that deep water (particularly in the deep South Atlantic) may have remained isolated for several thousand years after the

initial change in benthic δ^{18}O. Therefore, the benthic δ^{18}O signal in the deep South Atlantic may lag ice volume and the benthic δ^{18}O records of other sites. To evaluate whether the benthic δ^{18}O response at ODP 1090 [Hodell et al, 2003] was delayed during these two events, the benthic δ^{18}O-based age model is compared to one produced by aligning ODP 1090 planktonic δ^{18}O [Hodell et al, 2003] to the LR04 benthic stack. The planktonic and benthic age models agree very well except during the two failed terminations at 535 and 745 ka (Figure S4b). Thus, the benthic δ^{18}O response in the deep South Atlantic does appear to be delayed during these two events, consistent with the proposed lag between ice volume and pCO_2/deep water ventilation. For this reason, the planktonic δ^{18}O alignment is used for calculating the correlation of the alkenone proxy with pCO_2 (Table 1) and its phase relative to pCO_2 and the LR04 benthic δ^{18}O stack (Tables S2 and S3).

It is also worth noting that this planktonic δ^{18}O age model is nearly identical to the age model that Martínez-Garcia et al [2009] created by aligning ODP 1090 SST to Antarctic temperature on the EDC3_gas_a age model (Figure S4a). This provides additional support for my assertion that the LR04 and EDC3_gas_a age models differ by less than 3 kyr during terminations. Thus I conclude that, the different ages for benthic δ^{18}O and ice core pCO_2 responses during Termination 6 and MIS 18 are the result

of decoupling between the northern and southern hemispheres at this time rather than large errors in either age model.

5 Tropical SST and pCO_2

The tropical SST stack of Herbert et al. [2010] is constructed by stacking five detrended tropical SST records and then adding in the mean trend from 3.5–0 Ma of the three records which extend back to 3.5 Ma. These three sites are ODP 662, 722, and 846, which have trends of 0.65, 0.60, and 1.00 °C, respectively. If the temperature trends at all of these sites were primarily controlled by radiative forcing, then all three sites should have similar trends. Instead, Site 846 cools more than the other two, probably as the result of upwelling changes in the Eastern Equatorial Pacific (EEP). Therefore, Herbert et al. [2010] offer the following disclaimer about the stack's slope: "As this slope reflects only three estimates, one of which comes from the strongly cooling Eastern equatorial Pacific site 846, it may need to be revised downward as more long tropical SST records become available." (Herbert et al., 2010, Supporting Online Material, pg. 6).

Thus, it is reasonable to assume that some fraction of the stack's trend reflects the upwelling dynamics of the EEP and that the SST stack would better reflect changes in pCO_2 if its trend were based on one or more non-

upwelling sites. I adjust the stack to match the trend from ODP 806B in the Western Equatorial Pacific (WEP) warm pool because it is the continuous record least affected by upwelling and terrestrial influences. SST at ODP 806B has a trend of 0.61 °C/Myr from 1.35–0 Ma, which is similar to the trends at ODP 662 and 722. However, calculation of the mean linear trend of 806B SST and the SST stack is somewhat sensitive to noise and the exact age range evaluated. Therefore, I choose to characterize their trends using the change in mean SST from 0.5–0.1 Ma and 1.35–1.0 Ma. Site 806B cools by 0.48°C between these two time intervals (or 0.55°C/Myr), whereas the SST stack cools by 0.73°C (or 0.83 °C/Myr) (Figure S6). Thus, the slope of the SST stack should be reduced by 0.28°C/Myr to remove the long-term SST trend associated with upwelling changes at Site 846. However, the detrended SST stack could still contain the effects of abrupt upwelling changes, which would not be completely removed by adjusting the mean slope of the SST record.

References

Berger, W. H., T. Bickert, M. K. Yasuda, and G.Wefer (1996), Reconstruction of atmospheric CO2 from ice-core data and the deep-sea record of On-

tong Java plateau: The Milankovitch chron, Geol. Rundsch., 85, 466-495, doi:10.1007/BF02369003.

Bickert, T., W. H. Berger, S. Burke, H. Schmidt, and G. Wefer (1993), Late Quaternary stable isotope record of benthic foraminifers: Sites 805 and 806, Ontong Java plateau, Proc. Ocean Drill. Program Sci. Results, 130, 411-420.

Bickert, T., and G. Wefer (1996), Late Quaternary deep water circulation in the South Atlantic: Reconstruction from carbonate dissolution and benthic stable isotopes, in The South Atlantic: Present and Past Circulation, edited by G. Wefer et al., pp. 599-620, Springer, New York.

Duplessy, J. C., N. J. Shackleton, R. G. Fairbanks, L. Labeyrie, D. W. Oppo, and N. Kallel (1988), Deepwater source variations during the last climatic cycle and their impact on the global deepwater circulation, Paleoceanography, 3, 343–360.

Flower, B. P., D. W. Oppo, J. F. McManus, K. A. Venz, D. A. Hodell, and J. L. Cullen, North Atlantic intermediate to deep water circulation and chemical stratification during the past 1 Myr, Paleoceanography, 15, 388-403, 2000.

Grinsted, A., Moore, J. C. and Jevrejeva (2004), S. Application of the cross wavelet transform and wavelet coherence to geophysical time series. Nonlinear Process. Geophys. 11, 561–566.

Hodell, D. A., C. D. Charles, and F. J. Sierro (2001), Late Pleistocene evolution of the ocean's carbonate system, Earth and Planetary Science Letters, 192, 109–124.

Hodell, David A; Charles, Christopher D; Curtis, J H; Mortyn, P Graham; Ninnemann, Ulysses Silas; Venz, Kathryn A (2003), Data Report: Oxygen isotope stratigraphy of ODP Leg 117 sites 1088, 1089, 1090, 1093, and 1094. In: Gersonde, R., Hodell, D.A., and Blum, P. (eds.), Proceedings of the Ocean Drilling Program, Scientific Results, College Station, TX (Ocean Drilling Program), 177, 1–26 (online), doi:10.2973/odp.proc.sr.177.120.2003

Lisiecki, L. E., and M. E. Raymo (2005), A Pliocene-Pleistocene stack of 57 globally distributed benthic δ^{18}O records, Paleoceanography, 20, doi:10.1029/2004PA001071.

Lisiecki, L. E., and M. E. Raymo (2009), Diachronous benthic δ^{18}O responses during late Pleistocene terminations, Paleoceanography, 24, PA3210, doi:10.1029/2009PA001732.

Lisiecki, L. E. (2010) A simple mixing explanation for late Pleistocene changes in the Pacific-South Atlantic benthic δ^{13}C gradient, Clim. Past, 5, 2607-2630.

McIntyre, K., A. C. Ravelo, and M. L. Delaney (1999), North Atlantic Intermediate Waters in the late Pliocene to early Pleistocene, Paleoceanography, 14, 324–335.

McManus, J. F., D. W. Oppo, and J. L. Cullen (1999), A 0.5-million-year

record of millennial-scale climate variability in the North Atlantic, Science, 283, 971–974.

Mix, A. C., J. Le, and N. J. Shackleton (1995a), Benthic foraminiferal stable isotope stratigraphy from Site 846: 0–1.8 Ma, Proc. Ocean Drill. Program Sci. Results, 138, 839–847.

Mix, A. C., N. G. Pisias, W. Rugh, J. Wilson, A. Morey, and T. K. Hagelberg (1995b), Benthic foraminifer stable isotope record from Site 849 (0-5 Ma): Local and global climate changes, Proc. Ocean Drill. Program Sci. Results, 138, 371–412.

Oppo, D. W., McManus, J. F. and Cullen, J. C. Abrupt climate change events 500,000 to 340,000 years ago: evidence from subpolar North Atlantic sediments, Science, 279, 1335-1338, 1998.

Raymo, M. E., D. W. Oppo, B. P. Flower, D. A. Hodell, J. F. McManus, K. A. Venz, K. F. Kleiven, and K. McIntyre (2004), Stability of North Atlantic water masses in face of pronounced climate variability during the Pleistocene, Paleoceanography, 19, PA2008, doi:10.1029/2003PA000921.

Shackleton, N. J., and M. A. Hall, Oxygen and carbon isotope stratigraphy of DSDP Hole 552A: Plio-Pleistocene glacial history, Initial Rep. Deep Sea Drill. Project, 81, 599-609, 1984.

Shackleton, N. J., A. Berger, and W. R. Peltier, An alternative astronomical

calibration of the Lower Pleistocene timescale based on ODP Site 677, Trans. R. Soc. Edinburgh Earth Sci., 81, 251-261, 1990.

Shackleton, N. J., M. A. Hall, and D. Pate (1995), Pliocene stable isotope stratigraphy of ODP Site 846, Proc. Ocean Drill. Program Sci. Results, 138, 337–356.

Venz, K. A., D. A. Hodell, C. Stanton, and D. A. Warnke, A 1.0 Myr record of Glacial North Atlantic Intermediate Water variability from ODP site 982 in the northeast Atlantic, Paleoceanography, 14, 42-52, 1999.

Venz, K. A., and D. A. Hodell, New evidence for changes in Plio-Pleistocene deep water circulation from Southern Ocean ODP Leg 177 Site 1090, Palaeogeography, Palaeoclimatology, Palaeoecology, 182, 197-220, 2002.

Table S1: Core Locations

Core	Lat	Long	Depth (m)	Citation
North Atlantic				
DSDP 552	56.0	-23.2	2301	Shackleton and Hall, 1984
ODP 980/981	55.5	-14.7	2169	Oppo et al., 1998; McManus et al., 1999; Flower et al., 2000
ODP 982	57.5	-15.9	1145	Venz et al., 1999; Venz and Hodell, 2002
ODP 983	60.4	-23.6	1983	McIntyre et al., 1999; Raymo et al., 2004
South Atlantic				
ODP 1089	-40.9	9.9	4621	Hodell et al., 2001
ODP 1090	-42.9	8.9	3702	Venz and Hodell, 2002
GeoB1211	-24.5	7.5	4085	Bickert and Wefer, 1996
Pacific				
ODP 677	4.2	-83.7	3461	Shackleton et al., 1990
ODP 806B	0.3	159.4	2520	Berger et al., 1996; Bickert et al., 1993
ODP 846	-3.1	-90.8	3307	Mix et al., 1995a; Shackleton et al., 1995
ODP 849	0.2	-110.5	3851	Mix et al., 1995b

Table S2: Age model differences (EDC3_gas_a age - LR04 age)

Termination	Age (ka)	CO_2-$\Delta\delta^{13}C_{P-\frac{NA}{2}}$ (kyr)	CO_2-log[alk] (kyr)
T2	115–145	-1.4	-4.6
T3	235–255	1.5	-0.3
T4	325–348	2.4	-0.7
T5	406–442	-0.4	-0.4
T6	510–540	1.2	-4.5
T7	607–644	2.7	2.4
T8	695–723	-0.6	-5.3
MIS 18	728–752	2.4	-2.2
T9	783–798	-2.7	0.7

Table S3: Termination lags

Termination	Age (ka)	δ^{18}O-$\Delta\delta^{13}C_{P_\frac{NA}{2}}$ (kyr)	δ^{18}O-log[alk] (kyr)
T2	115–145	1.5	4.7
T3	235–255	0.2	3.3
T4	325–348	0.4	1.7
T5	403–438	2.7	3.6
T6	523–549	-9.8	-2.6
T7	609–644	1.3	2.4
T8	695–723	1.6	7.3
MIS 18	728–755	-3.5	-1.3
T9	778–799	3.7	0.5

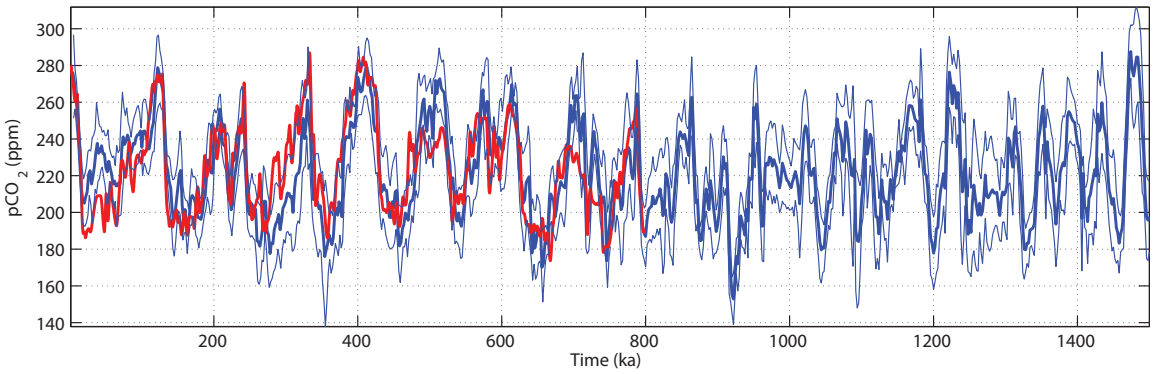

Figure S1: Ice core pCO_2 (red) and scaled $\Delta\delta^{13}C_{P\_\frac{NA}{2}}$(thick blue) with 1-$\sigma$ uncertainty range (thin blue).

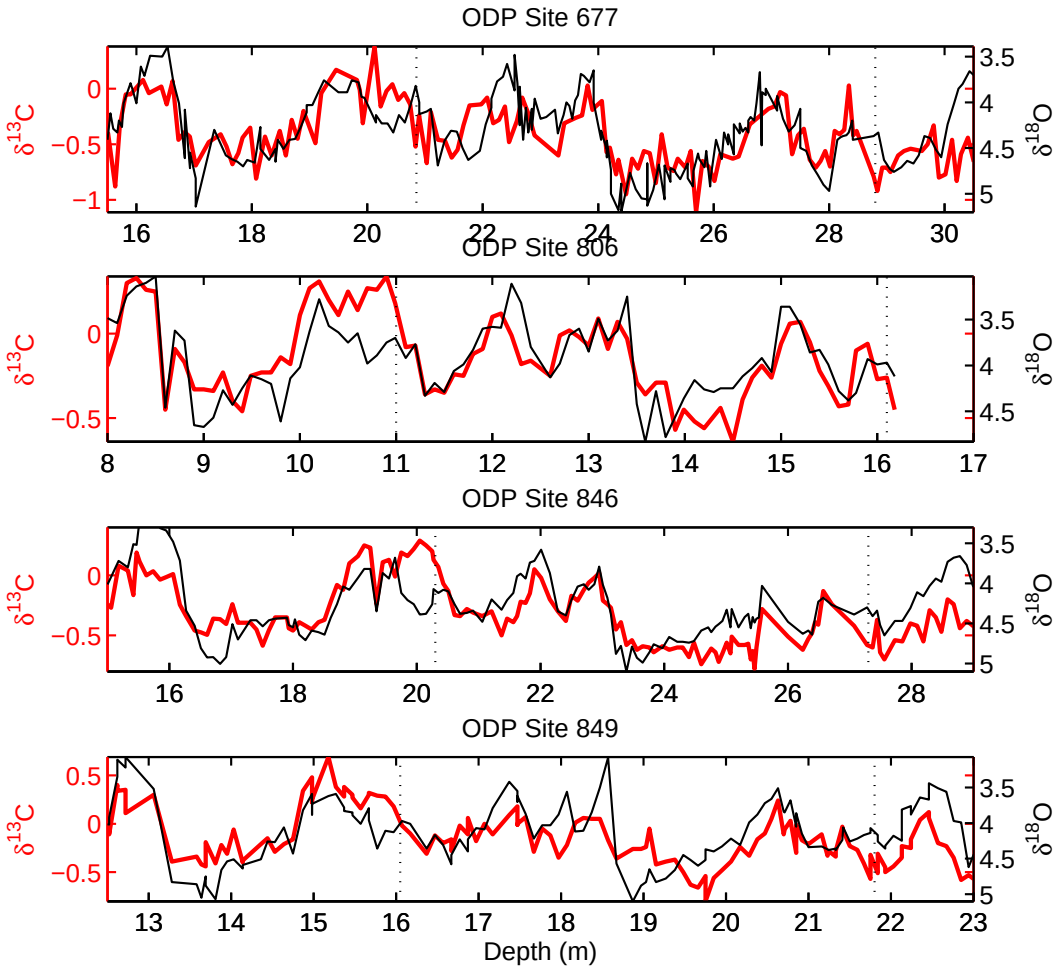

Figure S2: Benthic δ^{18}O (black) and δ^{13}C (red) in Pacific cores ODP 677, 806B, 846, and 849. Vertical dotted lines mark the two failed terminations where δ^{13}C lags δ^{18}O.

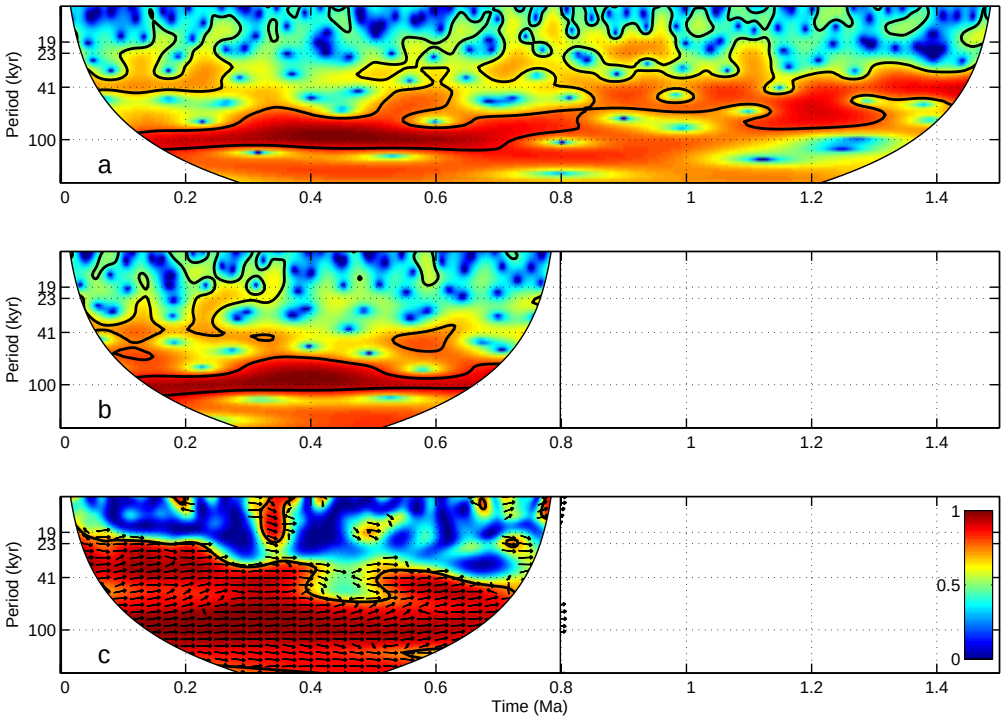

Figure S3: Wavelet power spectra of $\Delta\delta^{13}C_{P_\frac{NA}{2}}$and CO_2. Local wavelet power spectra of (a) $\Delta\delta^{13}C_{P\_\frac{NA}{2}}$ and (b) CO_2 [Lüthi et al, 2008]. (c) Coherence between $\Delta\delta^{13}C_{P\_\frac{NA}{2}}$ and CO_2. Arrows indicate the relative phase with right indicating an in-phase response and down indicating a $\Delta\delta^{13}C_{P\_\frac{NA}{2}}$ lag. Because the two records are compared using their respective age models, the phase estimates are affected by age model difference. In all three plots, black contours mark the 5% significance level against red noise.

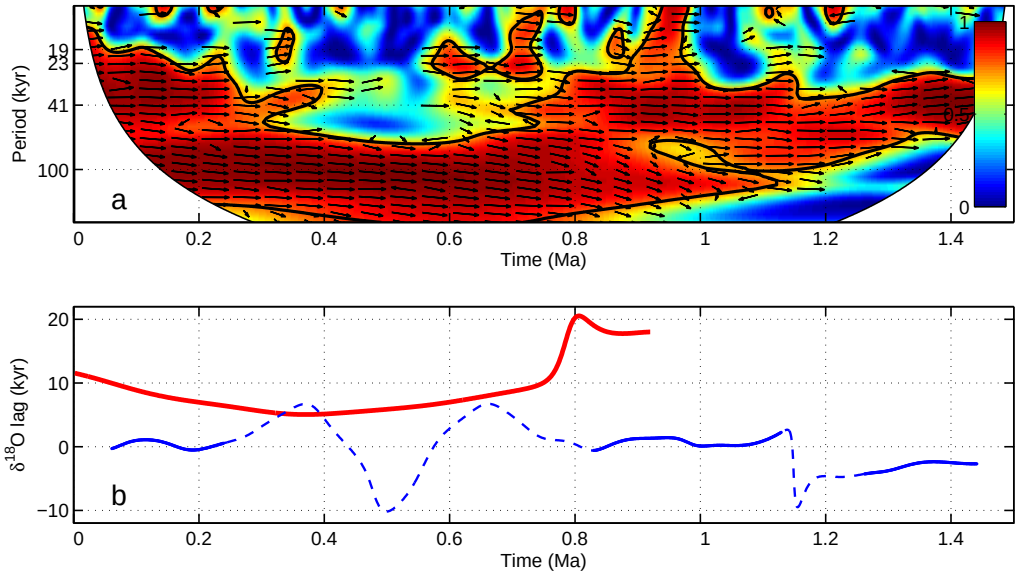

Figure S4: Wavelet cross-spectral analysis of $\Delta\delta^{13}\mathrm{C}_{P_\frac{NA}{2}}$and benthic δ^{18}O. (a) Coherence between $\Delta\delta^{13}\mathrm{C}_{P-\frac{NA}{2}}$ and benthic δ^{18}O. A black contour marks the 5% significance level against red noise. Arrows indicate the relative phase with down indicating a δ^{18}O lag. Because both records are on the LR04 age model, the phase estimates indicate real differences in the timing of $\Delta\delta^{13}\mathrm{C}_{P-\frac{NA}{2}}$ and δ^{18}O response. (b) δ^{18}O phase lag relative to $\Delta\delta^{13}\mathrm{C}_{P-\frac{NA}{2}}$ for the 100-kyr cycle (red) and 41-kyr cycle (blue). Solid (dotted) lines indicate phase estimates for time intervals with coherence greater (less) than 0.85.

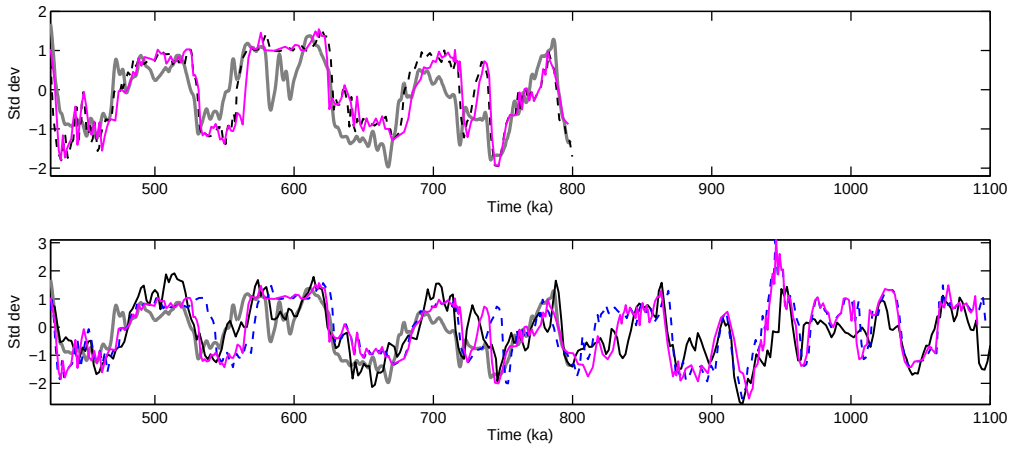

Figure S5: Comparison of different age models for ODP 1090. pCO_2 (gray), $\Delta\delta^{13}C_{P-\frac{NA}{2}}$ (black, lower panel), and minus the logarithm of ODP 1090 alkenone concentration using age models derived from alignment of: (1) ODP 1090 SST to Antarctic temperature on the EDC3 age model [Martínez-Garcia,2009] (black dotted, upper panel), (2) ODP 1090 planktonic $\delta^{18}O$ to the LR04 benthic $\delta^{18}O$ stack (pink, both panels), and (3) ODP 1090 benthic $\delta^{18}O$ to the LR04 benthic $\delta^{18}O$ stack (blue dotted, lower panel). All time series are scaled to zero mean and unit standard deviation.

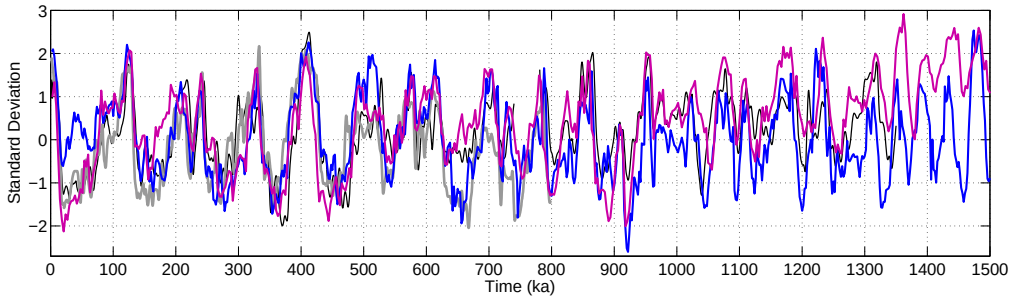

Figure S6: Tropical SST and pCO_2. a) Ice core pCO_2 (thick gray) compared to $\Delta\delta^{13}C_{P-\frac{NA}{2}}$ (blue), SST at ODP 806B [Medina-Elizalde and Lea, 2005] (black) and a tropical SST stack [Herbert et al, 2010] (purple). Records are scaled to zero mean and unit standard deviation from 100-500 ka, but trends are not adjusted.